JOHNS HOPKINS
APPLIED PHYSICS LABORATORY

NIAC
NASA Innovative Advanced Concpts

Swarm Flyby Gravimetry

NIAC Phase I Report

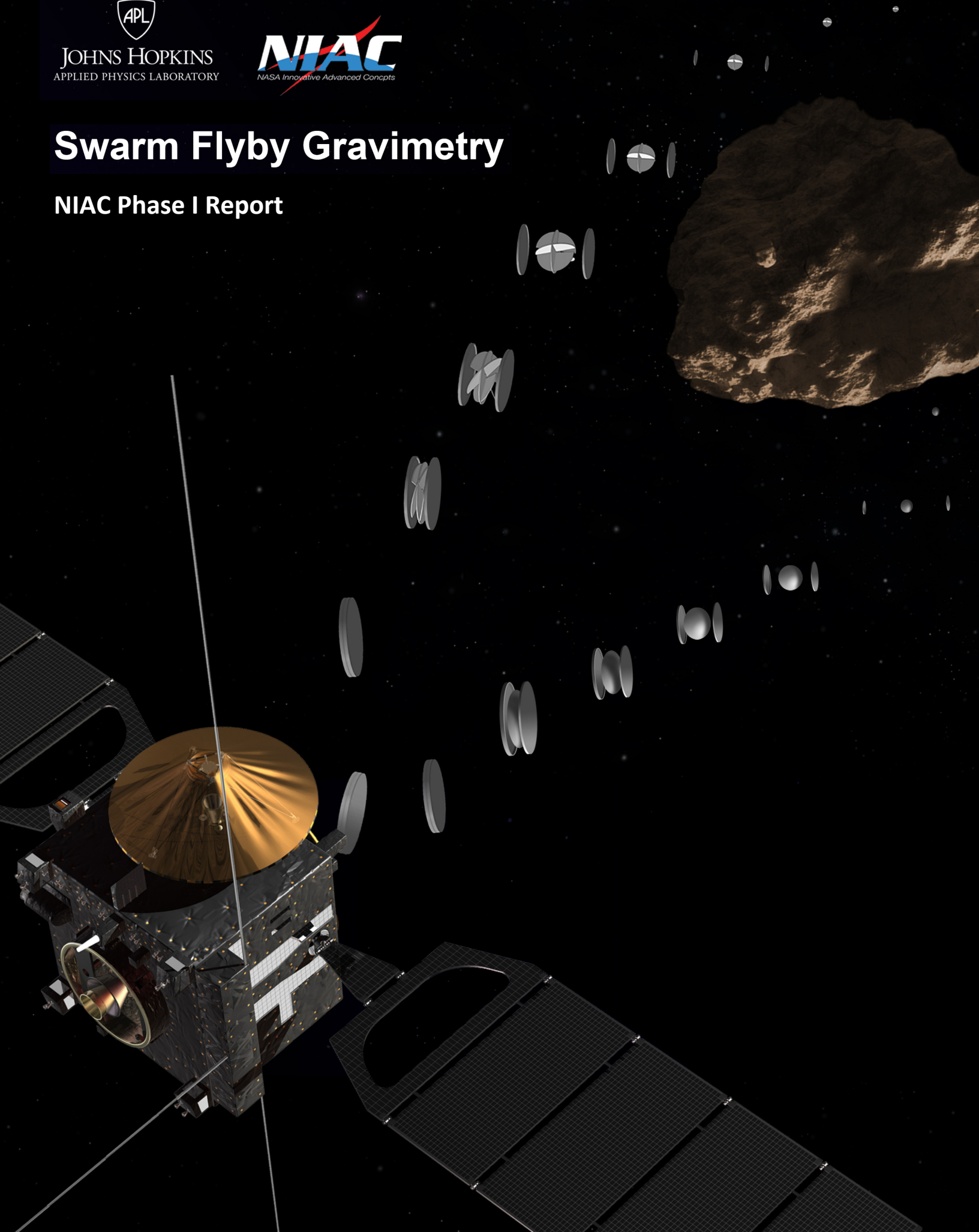

Swarm Flyby Gravimetry

NIAC Phase I Final Report

NNH14ZOA001N, NIAC14B

April 01, 2015

The Johns Hopkins University Applied Physics Laboratory

Fellow: Dr. Justin Atchison
Co-I: Dr. Ryan Mitch
Project Scientist: Dr. Andy Rivkin

1 Executive Summary

This study describes a new technology for discerning the gravity fields and mass distribution of a solar system small body, without requiring dedicated orbiters or landers. Instead of a lander, a spacecraft releases a collection of small, simple probes during a flyby past an asteroid or comet. By tracking those probes from the host spacecraft, one can estimate the asteroid's gravity field and infer its underlying composition and structure. This approach offers a diverse measurement set, equivalent to planning and executing many independent and unique flyby encounters of a single spacecraft. This report assesses a feasible hardware implementation, derives the underlying models, and analyzes the performance of this concept via simulation.

In terms of hardware, a small, low mass, low cost implementation is presented, which consists of a dispenser and probes. The dispenser constains roughly 12 probes in a tube and has a total size commensurate with a 6U P-Pod. The probes are housed in disc shaped sabots. When commanded, the dispenser ejects the top-most probe using a linear motor. The ejected probe separates from its sabots and unfolds using internal springs. There are two types of probes, each designed for a particular tracking modality. The reflective probe type, tracked by a telescope, unfolds to form a diffusely reflective sphere. The retroreflector probe type, tracked by a lidar, unfolds to form a corner-cube retroreflector assembly. Both types are designed to spherical so that their attitude doesn't affect the spacecraft's tracking performance.

This analysis indicates that the point-mass term of small bodies larger than roughly 500 m in diameter can be observed from a host spacecraft that tracks locally deployed probes throughout a flyby to an uncertainty of better than 5%. The conditions by which this measurement is possible depends on the characteristics of the asteroid (size, type), the flyby velocity, and the type of tracking available (angles-only or angles+ranging). For most encounters, a few (1-3) well placed probes can be very effective, with marginal improvement for additional probes. Given realistic deployment errors, an encounter may require roughly 10-12 probes to ensure that 1-3 achieve their target. Long duration tracking of probes flying by large asteroids (>5 km diameter) can sometimes provide observability of the gravity field's first spherical harmonic, J_2. In summary, this method offers a feasible, affordable approach to enabling or augmenting flyby science.

Contents

2 Introduction

Asteroid gravimetry has important relevance to space-science, planetary defense, and future human spaceflight. Gravimetry gives insight into an asteroid or comet's internal composition and structure, which cannot be studied by imagers, spectrometers, or even surface samplers. It has implications for the formation models of our solar system, since many small bodies are thought to be remnants of the solar system's early states. Consolmagno, Britt, and Macke[1] suggest that just knowing an asteroid's or comet's density and porosity can give important insights into the early solar system's accretional and collisional environment. Asteroid gravimetry also has implications for human spaceflight since near-Earth objects are considered as targets for human exploration. There is a need to characterize our near-Earth neighborhood in order to select candidate targets and assess their expected material properties. There is value in being able to confidently predict how different handling, anchoring, or landing approaches will operate on a particular class of target. Likewise, small body compositional and structural knowledge is required for many proposed missions to mitigate asteroid impacts at Earth. For example, an asteroid's response to an impactor will depend principally on its interior composition and mechanical properties. Asteroid interior data may suggest that certain classes of asteroids would be more safely diverted using other concepts, such as gravitational tugs. Asteroid composition models will improve the fidelity of asteroid-Earth impact predictions and thus provide a more complete understanding of the risks posed by different asteroids.

A body's gravity is typically observed by measuring its effect on the trajectory of a smaller neighbor, such as a moon or spacecraft.[2] That is, by tracking the moon or spacecraft's motion, one can estimate properties of the object's gravitational field. If the gravitational effects are observable, then the quality of the estimate depends on the number, geometric diversity, and accuracy of the tracking measurements. For small bodies, these measurements are difficult to attain. Few asteroids have companions that can be tracked, so we have to rely on observations of spacecraft for high accuracy results. This is achieved by maneuvering a spacecraft to fly past, orbit, or land on a small body while tracking the spacecraft from the ground. While orbiters and landers offer the highest quality science, they require dedicated missions and are often constrained to a single target due to practical Δv limitations.

Flybys are favorable because they are often easily added to existing mission designs with little impact to cost or operations;[3,4] however, they present many challenges for gravimetry. Flybys are typically short-lived events owing to relative velocities of many km/s. The magnitude of deflection from an asteroid is a function of the mass of the asteroid, the asteroid-spacecraft relative velocity, and close-approach range to the center-of-mass. For typical relative velocities (5-15 km/s) the spacecraft must pass very close to the asteroid to achieve a measurable deflection. The high relative velocity implies a short-time-duration conjunction and the asteroid exerts only a weak gravitational force that diminishes in proportion to r^{-2}. The close proximity represents a risk, or operations challenge, to the mission. In addition, low-altitude passes may degrade the science from other instruments that cannot accommodate the high spacecraft slew rates required to track the object during a close pass (e.g., cameras or spectrometers).

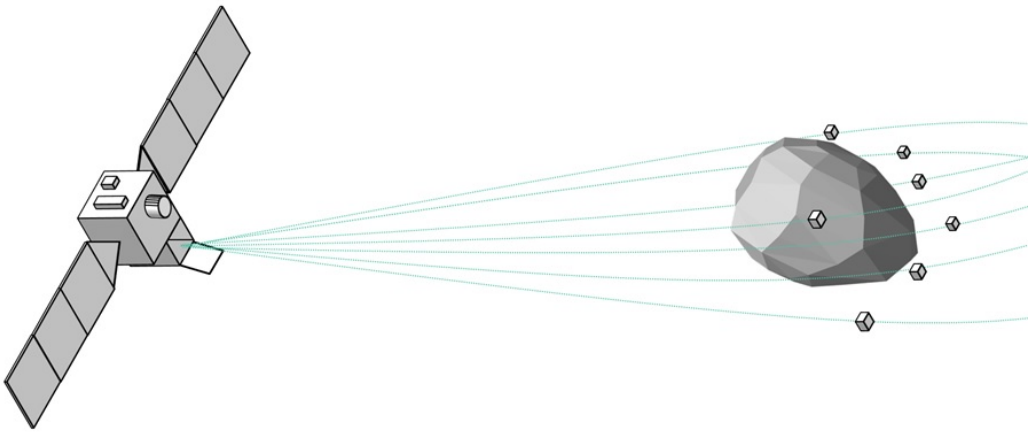

Figure 1: Spacecraft flyby of an asteroid with the spacecraft tracking its ejected probes.

This paper describes a method to enable or augment gravimetry during flybys of small-bodies without imposing a low-altitude spacecraft flyby. Instead, the spacecraft acts a host to a group of small deployable probes,[5,6] as shown in Figure 1. The host spacecraft releases the probes just prior to a flyby. The probes diverge from the host and pass the small body from a variety of ranges and directions. Each probe's motion represents an independent flyby. The host spacecraft tracks each probe's pre- and post-encounter relative positions and downlinks this data to the ground. Once the measurements are received, an estimation technique is used to solve for the best-fit orbit parameters and the small body's mass. Given a large quantity of probes and a rich diversity of probe trajectories, this solution can have sufficient fidelity to yield a gravity model. Combining this model with a surface profile derived from optical or altimeter measurements may give insight into the asteroid's mass distribution and composition.

This approach is similar to that studied by Grosch and Paetznick[7] and Psiaki[8] who used a set of relative measurements over a series of orbits to estimate the inertial position of deployed probes and the central body's gravitational terms. Likewise, Muller and Kachmar[9] analyzed the use of relative measurements of deployed probes to estimate inertial terms in a host spacecraft's dynamics.

The probes need only be trackable, which implies that they may be very simple, low-cost, and easily accommodated on-board a spacecraft. If properly deployed, they can yield many measurements among many independent paths, which improves the observability of the gravimetry problem. In addition, most measurement types benefit from short ranges, offering higher signal-to-noise measurements relative to the host spacecraft than could be achieved relative to an Earth based ground station. Finally, the probes can conceivably be deployed to pass within a very short range of the small body's surface, which allows the host spacecraft to maintain a safe distance that is optimal for other instruments. The probes' reduced magnitude of closest approach will yield a corresponding increase of their trajectory change when compared to that of the spacecraft. For a

nominally spherical asteroid of fixed mass, the efficacy of this technique is limited by the asteroid's *density*. Higher density asteroids will permit the probes to reduce their distance of closest approach (relative to the center-of-mass), thus increasing the asteroid's perturbation of the probes from their nominal trajectories and improving the accuracy of the estimation results.

This paper describes a set of candidate system architectures, including a variety of tracking methods and a candidate deployment technique, which are analyzed via simulation. The analysis includes a definition of the state vector, the dynamics model of the flyby, several different measurement models, an appropriate estimation algorithm, and a covariance simulation. The simulation and estimation approach are evaluated over a trade-space that assesses relevant parameters.

3 System Architecture

The system is composed of three principal components: the tracking method, the probe design, and the deployment method. A successful architecture addresses each of these components in a manner that results in high-quality gravimetry while imposing as few constraints or burdens on the host spacecraft or mission. The tracking method and probe design are tightly coupled and are presented together, while the deployment method is considered separately.

3.1 Tracking Method and Probe Design

The host spacecraft must detect and track each probe throughout the flyby. For large numbers of probes, the tracking method should ideally facilitate differentiation among the probes and measurement attribution. Alternatively, one could pursue multiple hypothesis models that would consider each measurement's association with each probe. Table 1 lists six candidate tracking methods. In addition to the parameters listed, the options also differ with respect to the required burdens to the host spacecraft and required complexity of the probe design. Each of these approaches is described in greater detail below.

Table 1: Candidate Tracking Methods

Sensing Type	Power Source	Measurement Type	Differentiation
Optical	Sunlight Reflection (Sun)	Angles	Challenging
	LED Illuminators (Battery)	Angles	Possible
	Laser Irradiation (Host Spacecraft)	Angles and Range	Built-In
Infrared	Powered Heaters (Battery)	Angles	Possible
Radio	RF Beacon (Solar, Battery)	Doppler and/or Range	Built-In
	Radar Reflection (Host Spacecraft)	Doppler and/or Range	Possible

1. **Sunlight Reflection** - One favorable candidate method requires that the probes be reflective to sunlight. The host-spacecraft then uses its on-board imager to detect and track the probes as they drift away from the spacecraft and flyby the small body. This approach requires a low solar phase angle (the angle connecting the sun-probe-imager points) so that the probes' reflections are visible to the spacecraft. This can be achieved by deploying the probes in the anti-sun direction. The reflection is dependent on the probe's shape, size, and reflectivity properties.

2. **LED Illuminators** - In this method, light-emitting-diodes (LED) are tracked by their optical signature. These can operate independently of the sun-relative geometry. The probes would consist of batteries and flashing LEDs. Here, the probes' detectability depends on the number and brightness of LEDs. This is reminiscent of the Japanese FITSAT-1 cubesat,[10] which was

observable at ranges of 100's of kilometers using standard telescopes with long integration times.

3. **Lidar** - Ranging lasers were used on the Gravity Recovery and Climate Experiment[11] (GRACE) and Gravity and Interior Laboratory[12] (GRAIL) missions. This implementation offers the highest quality measurements, but imposes requirements on the host spacecraft, which must accommodate and point a laser. In this instantiation, the probes could consist of assemblies of corner-cube retroreflectors,[13,14] which would give very high returns at nearly any attitude. This would help to mitigate the losses associated with range (d^{-4}). It may be possible to use an existing laser altimeter designed for surface science.

4. **Powered Heaters** - If the host spacecraft carries a focal plane sensitive to infrared wavelengths, it may be possible to detect heated probes' thermal signatures. The performance and duration of the probes are limited by the available on-board power storage. For practical battery sizes, the effective tracking range is relatively short. In addition, the tracking accuracy is likely low given the poorer relative quality of available infrared focal plane arrays.

5. **Radio Frequency (RF) Beacons** - If each probe is equipped with a radio-frequency beacon, it could be readily identifiable with an on-board radio subsystem. Differentiation would be straightforward via time-division, channel-division, or code-division multiple access approaches. One likely challenge is the measurement quality associated with an on-board oscillator. The change in relative velocity is quite small between the probes and the host-spacecraft. This requires a very stable probe oscillator during the whole encounter. Otherwise, thermal variation in the oscillator could overpower any induced frequency variation.

6. **Radar Reflectors** - If each probe is reflective in an RF sense, it may be possible to detect and track very simple probes over long ranges using a radar instrument on the host spacecraft. Here, the signature is defined by the probe's radar cross section. One probe implementation could consist of simple metal dipoles,[15] as is used in radar chaff or was used in Project West Ford.[16] A higher return design would use corner cube retroreflector[13] assemblies.[14] The longer wavelength of the radar signal eases the probe's reflection and flatness tolerances, which facilitates production. This approach burdens the host spacecraft with carrying a dedicated radar payload, of which many space-qualified designs currently exist.

Two feasible deployable probe concepts were designed. The first probe design addresses the sunlight-reflection case and constitutes of an expanding, 10 cm diffuse sphere. The exterior is a white fabric wrapping a thin spring-metal frame. When compact, the probe fits in between two sabots, which house it prior to ejection. This is illustrated in Figure 2.

The second probe design applies to the lidar and radar tracking methods. This design consists of a central mirrored disc, with 8 unfolding mirrored sides. The compacted shape is a thin disc that fits within two sabots. Once the sabots are removed, the probe's sides unfolded (via torsion springs), and the assembly consists of 8 corner-cube retroreflectors as illustrated in Figure 2.

Both probe designs are spherical, such that they give a high signal-to-noise return in any orientation. Additionally, this facilitates the characterization, calibration, and estimation of solar radiation pressure, which is treated as an error source in this analysis.

3.2 Deployment

The host spacecraft must release each probe onto a trajectory that passes within a short range of the target body along an independent, diverse path without subsequently interfering with the host spacecraft. Given the very low values of imparted Δv by the low-mass small-bodies, the probability of a probe recontacting the spacecraft is insignificant.

A favorable deployment architecture consists of a combination of spacecraft pointing, spacecraft thrusting, and a hardware deployment mechanism. Multi-payload deployment has been demonstrated with cubesats, which are routinely deployed from launch vehicle upper stages without interfering with the primary mission payloads. Here, the vehicle points the cubesat's compressed-spring deployer along a desired direction, releases a stop that allows a spring to extend and impart a relative separation velocity to the cubesat, and then executes a small collision avoidance maneuver to prevent any future recontacts. This process would be useful for the flyby application as well, in that the deployment benefits from the spacecraft's high-quality attitude control and timing, to place the probe on a low-altitude pass of the small body. Compression springs introduce a non-negligible level of uncertainty to the deployment. As an alternative, a small controllable solenoid could be commanded to eject each probe. An accurate deployment process would include extensive pre-launch component characterization, and it would include a study of performance degradation due to the long storage times between assembly, launch, and use.

A dispenser has been designed to accommodate the two types of probes. The dispenser consists of a tube that contains roughly 12 probe assemblies. The probes are contained within low-friction disc sabots. When commanded, the top-most probe assembly is ejected using a linear motor. The motor pushes the probe assembly completely out of the "chamber" and then returns to a rest-state. The next probe assembly is then pushed into place for ejection by a compression spring. The size (35 cm x 25 cm x 15 cm) and mass (< 8 kg) of the dispenser is meant to be commensurate with a 6U P-Pod CubeSat deployer. The linear motor requires 20-200 W of power at the time of ejection. The housing and sabots were rapid-prototyped, as shown in Figure 3.

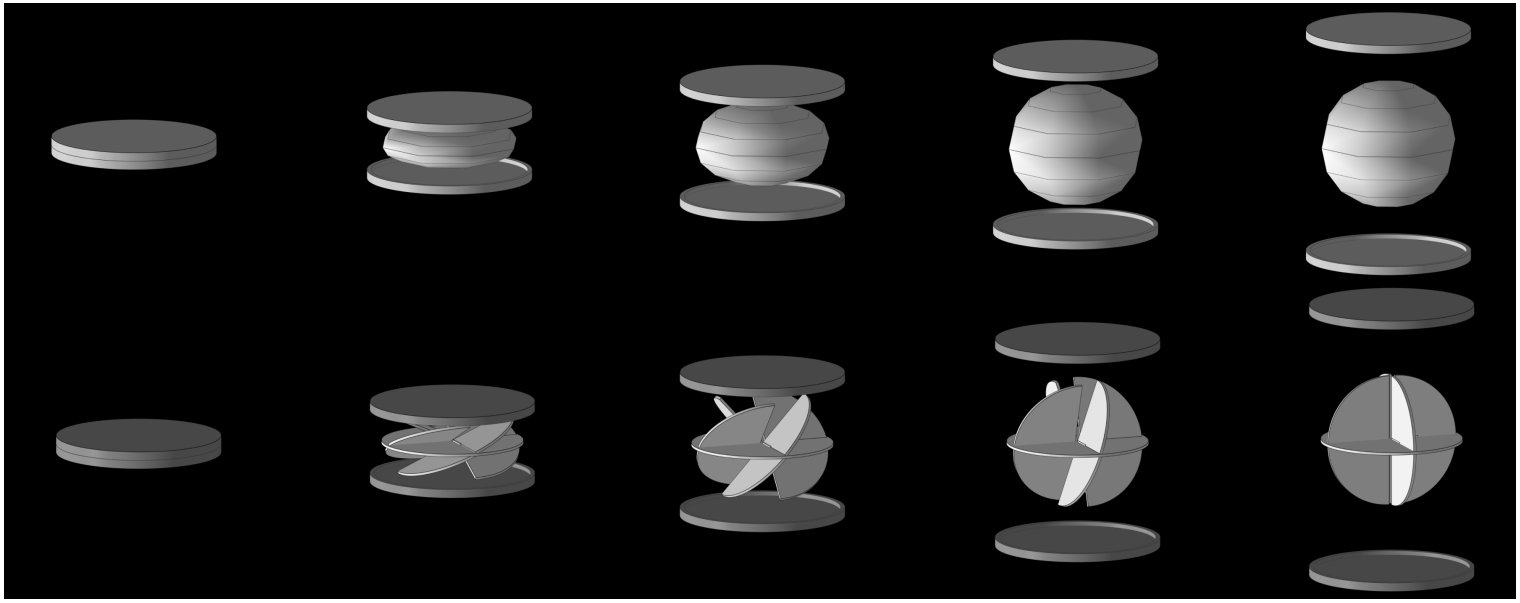

Figure 2: Conceptual designs for dispensed optically reflective probe (top) and corner-cube retroreflector probe (bottom).

Figure 3: Photograph of dispenser concept prototype.

4 Analysis

4.1 System State Definition

The following analysis is based on models of the probes, host spacecraft, and the asteroid. The parameters that define these models are referred to as the states of the system. These states can be combined to form one system state vector with the following definition:

$$X = \left[\ \underline{r}_1 \ , \ \underline{r}_2 \ , \ \cdots \ , \ \underline{r}_N \ \middle| \ \underline{\dot{r}}_1 \ , \ \underline{\dot{r}}_2 \ , \ \cdots \ , \ \underline{\dot{r}}_N \ \middle| \ g_1 \ , \ g_2 \ , \ \cdots \ , \ g_M \ \right]^T \tag{1}$$

where $\underline{r}_i$ is the 3-by-1 position vector of probe i for $i = 1$–N, $\underline{\dot{r}}_i$ is the 3-by-1 velocity vector of probe i, g_j is the j^{th} coefficient of a yet-to-be-defined parameterization of the asteroid gravitational field for $j = 1$–M, and $*^T$ is the transpose of the quantity $*$. The terms $\underline{r}_i$ and $\underline{\dot{r}}_i$ are defined as:

$$\underline{r}_i = [x_i \ \ y_i \ \ z_i]^T \tag{2}$$

$$\underline{\dot{r}}_i = [\dot{x}_i \ \ \dot{y}_i \ \ \dot{z}_i]^T \tag{3}$$

The selection of the reference frame and the gravity model are deferred until the next subsection.

The following analysis is based on two different types of state-space models:[17] a dynamics model and a measurement model. The dynamics model describes the way that all of the states change over time, and the measurement model defines the functional dependence of the measurements on those same states.

4.2 System Dynamics

The dynamics of the probes are modeled as obeying the following equation:

$$\underline{\ddot{r}} = f\left(\underline{r}\right) + \underline{d} \tag{4}$$

where $\underline{\ddot{r}}$ is the second time derivative of the position vector $\underline{r}$, $f\left(\underline{r}\right)$ is the position dependent gravitational acceleration, and $\underline{d}$ is the acceleration term associated with all other perturbations, including solar gravity, n-body gravity, and solar radiation pressure.

The secondary accelerations modeled by $\underline{d}$, while non-negligible, are treated as constant over the period of the flyby encounter among all the probes. This assumes that the value of these terms is insensitive to variation in each probe's local position over the encounter. In the case of solar radiation pressure, this assumes that a campaign was conducted to characterize the optical parameters for each probe prior to launch. Alternatively, the probes can be designed such that the solar radiation pressure acting on each probe is attitude-independent and consistent among all of the probes.

This work uses the center of mass of the asteroid as the center of its coordinate system. For this analysis, g_j consists of the first M coefficients in a spherical harmonic expansion.

The system state vector's nonlinear time derivative is:

$$\dot{X} = \left[\begin{array}{c|c|c|c} \underline{\dot{r}}_1 \ , \ \underline{\dot{r}}_2 \ , \ \cdots \ , \ \underline{\dot{r}}_N & f\left(\underline{r}_1\right) \ , \ f\left(\underline{r}_2\right) \ , \ \cdots \ , \ f\left(\underline{r}_N\right) & 0_{1\times M} \end{array} \right]^T \tag{5}$$

where the bottom subvector indicates that the gravitational parameters are constant throughout the simulation. $f\left(\underline{r}_i\right)$ is a 3-by-1 vector that represents the computation of the small body's nonlinear position-dependent gravitational acceleration for the i^{th} probe.

The system state vector's Jacobian $A = \partial\dot{X}/\partial X$, which is necessary to compute the model's state-transition-matrix, takes the form:

$$A = \left[\begin{array}{c|c|c} \left[\frac{\partial \underline{\dot{r}}_i}{\partial \underline{r}_i}\right] & \left[\frac{\partial \underline{\dot{r}}_i}{\partial \underline{\dot{r}}_i}\right] & \left[\frac{\partial \underline{\dot{r}}_i}{\partial g_j}\right] \\ \hline \left[\frac{\partial \underline{\ddot{r}}_i}{\partial \underline{r}_i}\right] & \left[\frac{\partial \underline{\ddot{r}}_i}{\partial \underline{\dot{r}}_i}\right] & \left[\frac{\partial \underline{\ddot{r}}_i}{\partial g_j}\right] \\ \hline \left[\frac{\partial \dot{g}_j}{\partial \underline{r}_i}\right] & \left[\frac{\partial \dot{g}_j}{\partial \underline{\dot{r}}_i}\right] & \left[\frac{\partial \dot{g}_j}{\partial g_j}\right] \end{array} \right] \tag{6}$$

Recognizing that gravity is dependent on position only, and that the gravitational parameters are constant, many of these terms simplify:

$$A = \left[\begin{array}{c|c|c} 0_{(3N\times 3N)} & I_{(3N\times 3N)} & 0_{(3N\times M)} \\ \hline \left[\frac{\partial \underline{\ddot{r}}_i}{\partial \underline{r}_i}\right] & 0_{(3N\times 3N)} & \left[\frac{\partial \underline{\ddot{r}}_i}{\partial g_j}\right] \\ \hline 0_{(M\times 3N)} & 0_{(M\times 3N)} & 0_{(M\times M)} \end{array} \right] \tag{7}$$

and where:

$$\left[\frac{\partial \underline{\ddot{r}}_i}{\partial \underline{r}_i}\right] = \left[\begin{array}{cccc} \left[\frac{\partial f(\underline{r}_1)}{\partial \underline{r}_1}\right] & 0_{3\times 3} & \cdots & 0_{3\times 3} \\ 0_{3\times 3} & \left[\frac{\partial f(\underline{r}_2)}{\partial \underline{r}_2}\right] & \ddots & \vdots \\ \vdots & \ddots & \ddots & 0_{3\times 3} \\ 0_{3\times 3} & \cdots & 0_{3\times 3} & \left[\frac{\partial f(\underline{r}_N)}{\partial \underline{r}_N}\right] \end{array} \right] \tag{8}$$

$$\left[\frac{\partial \underline{\ddot{r}}_i}{\partial g_j}\right] = \left[\begin{array}{cccc} \left[\frac{\partial f(\underline{r}_1)}{\partial g_1}\right] & \left[\frac{\partial f(\underline{r}_1)}{\partial g_2}\right] & \cdots & \left[\frac{\partial f(\underline{r}_1)}{\partial g_M}\right] \\ \left[\frac{\partial f(\underline{r}_2)}{\partial g_1}\right] & \left[\frac{\partial f(\underline{r}_2)}{\partial g_2}\right] & \cdots & \left[\frac{\partial f(\underline{r}_2)}{\partial g_M}\right] \\ \vdots & \vdots & \ddots & \vdots \\ \left[\frac{\partial f(\underline{r}_N)}{\partial g_1}\right] & \left[\frac{\partial f(\underline{r}_N)}{\partial g_2}\right] & \cdots & \left[\frac{\partial f(\underline{r}_N)}{\partial g_M}\right] \end{array} \right] \tag{9}$$

Here, $\left[\frac{\partial f(\underline{r}_i)}{\partial \underline{r}_i}\right]$ is the 3-by-3 matrix that represents the linearization of the i^{th} probe's gravitational acceleration as a function of its position $\underline{r}_i$. The matrix $\left[\frac{\partial \underline{\ddot{r}}_i}{\partial \underline{r}_i}\right]$ is diagonal because every probe is assumed to have a negligible gravitational attraction on every other probe.

As an example, for the point-mass case: $M = 1$, $g_1 = \mu$, $f(\underline{r}_i) = -\mu \underline{r}_i / \|\underline{r}_i\|^3$, the linearization is defined as

$$\left[\frac{\partial f(\underline{r}_i)}{\partial \underline{r}_i}\right] = \frac{-\mu}{\|\underline{r}_i\|^3} I_{3\times 3} + \frac{3\mu}{\|\underline{r}_i\|^5} \begin{bmatrix} x_i^2 & x_i y_i & x_i z_i \\ x_i y_i & y_i^2 & y_i z_i \\ x_i z_i & y_i z_i & z_i^2 \end{bmatrix} \tag{10}$$

$$\left[\frac{\partial f(\underline{r}_i)}{\partial g_j}\right] = \frac{-1}{\|r_i\|^3} \begin{bmatrix} x_i \\ y_i \\ z_i \end{bmatrix} \tag{11}$$

Models and linearizations for spherical harmonic representations of gravity, such as J_2, are available in Ref. [18].

The propagation from one time to another, say t_k to t_{k+1}, is defined using the standard linear systems equations:

$$X_{k+1} = \Phi\left(t_{k+1}, t_k, X_k\right) X_k \tag{12}$$

where it has been assumed that there is no process noise or control inputs perturbing the state, and Φ is the state-transition matrix. The inclusion of X_k in Equation (12) denotes a nonlinear dependence on the state vector. The matrix Φ can be computed using any one of a variety of numerical integration techniques.[19,20,21]

4.3 Measurement Models

The six different tracking methods presented earlier in this paper are categorized by measurement type as either angles, range, or Doppler shift. This section presents models of the measurements' dependence on components of the state vector X. There are multiple hardware designs that can produce each of the following measurement types, and the following measurement models are appropriate for a very wide range of design possibilities.

4.3.1 Angles

Four different tracking methods can generate angle-type measurements: sunlight reflection, LED illumination, lidar, and powered heaters. The observable quantities in these tracking methods are the azimuth (θ) and elevation (ϕ) angles. The model of the functional dependence of these measurements on the state vector is the following:

$$\theta_i = \tan^{-1}\left(\frac{(y_i - y_H)}{(x_i - x_H)}\right) \tag{13}$$

$$\phi_i = \tan^{-1}\left(\frac{(z_i - z_H)}{\sqrt{(x_i - x_H)^2 + (y_i - y_H)^2}}\right) \tag{14}$$

where $*_H$ refers to the "host" spacecraft's quantity $*$.

Equations (13) and (14) are nonlinear functions of the probe states. Standard estimation techniques approximate the nonlinear equations with Taylor series expansions that are typically truncated after the first derivative. The resulting approximation is linearly dependent on the system state vector. Therefore, the partial derivatives of the above equations with respect to the state vectors are required:

$$\frac{\partial \theta_i}{\partial \underline{r}_i} = \begin{bmatrix} \frac{-(y_i - y_H)}{(x_i - x_H)^2 + (y_i - y_H)^2} \\ \frac{(x_i - x_H)}{(x_i - x_H)^2 + (y_i - y_H)^2} \\ 0 \end{bmatrix}^T \tag{15}$$

$$\frac{\partial \phi_i}{\partial \underline{r}_i} = \begin{bmatrix} \frac{-(x_i - x_H)(z_i - z_H)}{((x_i - x_H)^2 + (y_i - y_H)^2)\|\underline{r}_i - \underline{r}_H\|^2} \\ \frac{-(y_i - y_H)(z_i - z_H)}{((x_i - x_H)^2 + (y_i - y_H)^2)\|\underline{r}_i - \underline{r}_H\|^2} \\ \frac{\left((x_i - x_H)^2 + (y_i - y_H)^2\right)}{\|\underline{r}_i - \underline{r}_H\|^2} \end{bmatrix}^T \tag{16}$$

4.3.2 Range

Three different tracking methods can generate range-type measurements: lidar, RF beacons, and radar reflectors. The model of the functional dependence of the angle measurements on the state vector is the following:

$$\rho = \|\underline{r}_i - \underline{r}_H\| \tag{17}$$

with the resulting partial derivatives:

$$\frac{\partial \rho}{\partial \underline{r}_i} = \frac{[\underline{r}_i - \underline{r}_H]^T}{\rho} \tag{18}$$

4.3.3 Doppler Shift

Two different tracking methods can generate Doppler shift-type measurements: RF beacons and radar reflectors. The model of the functional dependence of these measurements on the state vector is the following:

$$p = (\underline{\dot{r}}_i - \underline{\dot{r}}_H)^T \underline{\hat{\rho}}_{iH} \tag{19}$$

where $\underline{\hat{\rho}}_{iH}$ is the line-of-sight unit-vector from the host to probe i.

The partial derivative of the Doppler-shift measurement with respect to the state vector is:

$$\frac{\partial p}{\partial \underline{\dot{r}}_i} = \frac{(\underline{\dot{r}}_i - \underline{\dot{r}}_H)^T}{\rho} - \frac{(\underline{r}_i - \underline{\dot{r}}_H)^T (\underline{r}_i - \underline{r}_H)}{\rho^3} (\underline{r}_i - \underline{r}_H)^T \tag{20}$$

$$\frac{\partial p}{\partial \underline{\dot{r}}_i} = \underline{\hat{\rho}}_{iH}^T \tag{21}$$

4.3.4 Line-Of-Sight Obscuration

It is possible that at some times the asteroid of interest will pass between the host spacecraft and a probe. During these times the host spacecraft will not be able to make measurements of the probe. This line-of-sight obscuration and resulting measurement loss has been included in the results presented in this paper. Fortunately, this obscuration is brief and causes a negligible loss in the total number of measurements.

4.3.5 Combined Measurement Model Formulation

The following mathematical formulation and subsequent explanation are facilitated by stacking the measurements by type into a combined column vector:

$$\underline{y} = [\theta_1 \ , \ \theta_2 \ , \ \dots \ , \ \theta_N \,|\, \phi_1 \ , \ \phi_2 \ , \ \dots \ , \ \phi_N \,|\, \rho_1 \ , \ \rho_2 \ , \ \dots \ , \ \rho_N \,|\, p_1 \ , \ p_2 \ , \ \dots \ , \ p_N]^T \tag{22}$$

with the corresponding linearized measurement model:

$$\underline{y} = HX + \underline{v} \tag{23}$$

where H is defined as:

$$H = \left[\begin{array}{c|c|c} \left[\frac{\partial \theta_k}{\partial \underline{r}_i}\right] & \left[\frac{\partial \theta_k}{\partial \underline{\dot{r}}_i}\right] & \left[\frac{\partial \theta_k}{\partial g_j}\right] \\ \hline \left[\frac{\partial \phi_k}{\partial \underline{r}_i}\right] & \left[\frac{\partial \phi_k}{\partial \underline{\dot{r}}_i}\right] & \left[\frac{\partial \phi_k}{\partial g_j}\right] \\ \hline \left[\frac{\partial \rho_k}{\partial \underline{r}_i}\right] & \left[\frac{\partial \rho_k}{\partial \underline{\dot{r}}_i}\right] & \left[\frac{\partial \rho_k}{\partial g_j}\right] \\ \hline \left[\frac{\partial p_k}{\partial \underline{r}_i}\right] & \left[\frac{\partial p_k}{\partial \underline{\dot{r}}_i}\right] & \left[\frac{\partial p_k}{\partial g_j}\right] \end{array}\right] = \left[\begin{array}{c|c|c} \left[\frac{\partial \theta_k}{\partial \underline{r}_i}\right] & 0_{P\times 3N} & 0_{P\times M} \\ \hline \left[\frac{\partial \phi_k}{\partial \underline{r}_i}\right] & 0_{P\times 3N} & 0_{P\times M} \\ \hline \left[\frac{\partial \rho_k}{\partial \underline{r}_i}\right] & 0_{P\times 3N} & 0_{P\times M} \\ \hline \left[\frac{\partial p_k}{\partial \underline{r}_i}\right] & \left[\frac{\partial p_k}{\partial \underline{\dot{r}}_i}\right] & 0_{P\times M} \end{array}\right] \tag{24}$$

and $\underline{v}$ is the measurement noise. The measurement noise statistics are approximated as zero-mean, white, and Gaussian: $\underline{v} \sim \mathcal{N}(\underline{0}, R)$. The covariance matrix R is assumed to be a diagonal matrix due to the uncorrelated noise between different probes and different measurement types:

$$R = \text{blockdiagonal}\,(R_\theta, R_\phi, R_\rho, R_p) \tag{25}$$

where:

$$R_* = \begin{bmatrix} \sigma_{*1}^2 & 0 & \dots & 0 \\ 0 & \sigma_{*2}^2 & \ddots & \vdots \\ \vdots & \ddots & \ddots & 0 \\ 0 & \dots & 0 & \sigma_{*N}^2 \end{bmatrix} \tag{26}$$

and with each measurement having the same covariance ($\sigma_{*i} = \sigma_{*j}$).

If only a subset of the measurement types are used, eg., a camera *or* a radar, then the above equations would have the appropriate lines eliminated.

4.4 Simulation and Estimator

This paper's simulation assumes that no process noise and no control inputs perturb the state vector. Therefore, the system's behavior is fully defined by the initial state vector. This formulation suggests that a batch-type estimator should be used for state estimation. This work estimated the state vector X using a Maximum *A-Posteriori* batch estimator that is similar to the algorithm of Tapley, Schulz, and Born.[22] The Maximum *A-Posteriori* estimator requires an initial state estimate and associated covariance. That initial state estimate is refined using the simulated measurements in a least square process.

4.4.1 Initialization and Prior Distribution

To initialize the estimator, the system's state vector covariance is required. If each probe's initial uncertainty is associated with the expected knowledge of the location and imparted separation velocity at the time of deployment, it can be represented using additive, zero-mean Gaussian errors.

$$\begin{bmatrix} \underline{r}_i \\ \underline{\dot{r}}_i \end{bmatrix}_{est} = \begin{bmatrix} \underline{r}_i \\ \underline{\dot{r}}_i \end{bmatrix}_{true} + \begin{bmatrix} e_{\underline{r}} \\ e_{\underline{\dot{r}}} \end{bmatrix} \tag{27}$$

If the position and velocity errors are uncorrelated and zero-mean, then the errors $e_{\underline{r}}$ and $e_{\underline{\dot{r}}}$ can be modeled as vector-valued Gaussian random variables:

$$e_{\underline{r}_i} \sim \mathcal{N}\left(\underline{0}, P_{\underline{r}_i}\right) \tag{28}$$

$$e_{\underline{\dot{r}}_i} \sim \mathcal{N}\left(\underline{0}, P_{\underline{\dot{r}}_i}\right) \tag{29}$$

where:

$$P_{\underline{r}_i} = \begin{bmatrix} \sigma_x^2 & 0 & 0 \\ 0 & \sigma_y^2 & 0 \\ 0 & 0 & \sigma_z^2 \end{bmatrix}_i \quad , \quad P_{\underline{\dot{r}}_i} = \begin{bmatrix} \sigma_{\dot{x}}^2 & 0 & 0 \\ 0 & \sigma_{\dot{y}}^2 & 0 \\ 0 & 0 & \sigma_{\dot{z}}^2 \end{bmatrix}_i \tag{30}$$

Likewise, the gravitational field uncertainty can be represented using additive zero-mean Gaussian errors with error covariance P_g.

An *a-priori* $(6N+M) \times (6N+M)$ system state uncertainty can then be constructed:

$$P = \text{blockdiagonal}\left(P_{\underline{r}_1}\ ,\ P_{\underline{r}_2}\ ,\ \ldots\ ,\ P_{\underline{r}_N}\ ,\ P_{\underline{\dot{r}}_1}\ ,\ P_{\underline{\dot{r}}_2}\ ,\ \ldots\ ,\ P_{\underline{\dot{r}}_N}\ ,\ P_g\right) \tag{31}$$

4.4.2 Estimation Algorithm Details

The derivation of the Maximum *A-Posteriori* batch estimator is provided in moderate detail in the next few paragraphs. However, more information can be found in the references[22,23] regarding similar estimators.

If the prior distribution and the measurement noise distribution are both modeled as vector-valued Gaussian random variables, then the likelihood function is given by:[22]

$$L = f\left(X_j|\underset{\sim}{\widetilde{y}}_1\ ,\ \underset{\sim}{\widetilde{y}}_2\ ,\ \cdots\ ,\ \underset{\sim}{\widetilde{y}}_j\right) = \frac{f\left(\underset{\sim}{\widetilde{y}}_j|X_j\right) f\left(X_j|\underset{\sim}{\widetilde{y}}_1,\ \underset{\sim}{\widetilde{y}}_2\ ,\ \cdots\ ,\ \underset{\sim}{\widetilde{y}}_{j-1}\right)}{f\left(\underset{\sim}{\widetilde{y}}_j\right)} \tag{32}$$

$$= \frac{1}{(2\pi)^{(l)/2}\left|\widetilde{R}_j\right|^{\frac{1}{2}}} e^{-\frac{1}{2}\left[\left(\underset{\sim}{\widetilde{y}}_j-\widetilde{H}_jX_j\right)^T R_j^{-1}\left(\underset{\sim}{\widetilde{y}}_j-\widetilde{H}_jX_j\right)\right]}\ldots$$
$$\frac{1}{(2\pi)^{(6N+M)/2}\left|P_j\right|^{\frac{1}{2}}} e^{-\frac{1}{2}\left[\left(X_j-\bar{X}_j\right)^T P_j^{-1}\left(X_j-\bar{X}_j\right)\right]} \frac{1}{f\left(\underset{\sim}{\widetilde{y}}_j\right)} \tag{33}$$

where $f(*)$ is the probability density function (pdf) of the quantity $*$ and l is the total number of measurements. The subscript js in Equations (32)–(33) indicate quantities associated with the state vector at the initial time. The $\widetilde{*}$ operator has been placed on $\underset{\sim}{y}_j$ and H_j to denote a stacking of all of the measurements and measurement sensitivity matrices through the simulation into a single quantity with l rows:

$$\underset{\sim}{\widetilde{y}}_j = \left[\underset{\sim}{y}_1\ ,\ \underset{\sim}{y}_2\ ,\ \cdots\ ,\ \underset{\sim}{y}_k\right]^T \tag{34}$$

$$\widetilde{H}_j = \begin{bmatrix} H(X_1)\Phi\left(t_1,t_0\right) \\ H(X_2)\Phi\left(t_2,t_0\right) \\ \vdots \\ H(X_k)\Phi\left(t_k,t_0\right) \end{bmatrix} \tag{35}$$

where measurements are assumed to be received k number of times and the H matrices' dependence on the state vector has been shown explicitly.

Equation (33) can now be optimized with respect to the state, i.e., we wish to select the state X with the highest likelihood. Maximization of Equation (33) is mathematically equivalent to the minimization of:

$$\mathrm{J}\left(X_j\right) = -2\ln\left(L\right) = \left(\underset{\sim}{\widetilde{y}}_j - \widetilde{H}_jX_j\right)^T \widetilde{R}_j^{-1}\left(\underset{\sim}{\widetilde{y}}_j - \widetilde{H}_jX_j\right) + \left(X_j - \bar{X}_j\right)^T P_j^{-1}\left(X_j - \bar{X}_j\right) \tag{36}$$

which is referred to as the Maximum *A-Posteriori* cost function. The optimization has the necessary condition that the first partial derivatives of $J\left(X_j\right)$ with respect to the state are zero at the optimum:

$$\frac{\partial \mathrm{J}\left(X_j\right)}{\partial X_j} = 0 \tag{37}$$

Equation (33) is a linearized version of a nonlinear function. This nonlinear function must be driven to zero to satisfy the optimization conditions. This requirement is commonly accomplished

with the Newton-Raphson technique for root-finding, where the function is approximated by its Taylor series expansion and then minimized in an iterative manner. Unfortunately, in addition to the Jacobian matrix this method requires the computation of the Hessian tensor because the Newton-Raphson method requires the computation of $\frac{\partial^2 \mathrm{J}(X_j)}{\partial X_j^2}$. It is common practice[22] to approximate the Hessian as zero. This is true when the solution to nonlinear cost function is very close to the optimum, under certain assumptions. This method is commonly referred to as the Gauss-Newton method. Although not explicitly stated, this appears to be the method used by Tapley, Schutz, and Born[22] to arrive at their estimator.

The above derivation results in an iterative procedure with the following solution for a given linearization state X_0^q:

$$X_0^{q+1} = \Delta X + X_0^q \tag{38}$$

$$\Delta X = \left[\widetilde{H}^T \widetilde{R}^{-1} \widetilde{H} + P^{-1}\right]^{-1} \left[\widetilde{H}^T \widetilde{R}^{-1} \left(\widetilde{\underline{y}} - \widetilde{H} X_0^q\right) + P^{-1}\left(X_0^q - \bar{X}_0\right)\right] \tag{39}$$

where X_0^q is updated after each iteration to the most recently determined X_0^{q+1}, and that is used to relinearize the dynamics and measurement equations that define $\widetilde{H}$ via Equation (35). Tapley, Schutz, and Born[22] discuss an efficient way to compute some of the terms in Equation (35).

This paper's algorithm diverges from Tapley, Schutz, and Born's algorithm at this point. One primary difference is that the state vector increment ΔX is guarded. The increment determined by the evaluation of Equation (39) is the result of a linear approximation that is valid in only some small region about the linearization point X_0^q. If the recommended perturbation is too large then the new state vector may fall far outside of the linearization validity range, and the resulting state vector X_0^{q+1} may actually be a poorer fit and have a higher cost than the previous state vector X_0^q. If this process is performed repeatedly, then the estimator may move within a region around the optimal solution, it may diverge, or it may oscillate. Convergence can be enforced by redefining the state vector step-size for use in an iterative procedure:

$$X_0^{q+1'} = \alpha \Delta X + X_0^q \tag{40}$$

where α starts at 1 and is halved until the resulting state vector estimate $X_0^{q+1'}$ produces a decreased cost when compared to the previous cost from X_0^q. Once a cost decrease is realized X_0^{q+1} is set equal to $X_0^{q+1'}$, and then the procedure starts again. However, this convergence procedure will only be successful if the initial state estimate is sufficiently close to the optimal state estimate. A discussion of the criteria used to terminate this iterative procedure is beyond the scope of this work, but more detail can be found in the References.[24]

4.4.3 Estimation Algorithm Summary

The estimation approach requires five steps:

1. Linearize the dynamics and measurement model equations about an initial state vector.
2. Map each measurement's "innovation" to initial time t_0 using the state transition matrix Φ.
3. Compute the state vector perturbation $\alpha\Delta X$ that reduces the cost function $J(X_j)$.
4. Update the state vector estimate using $\alpha\Delta X$ and relinearize the necessary equations.
5. Repeat steps 2-4 until the nonlinear iteration convergence criteria are satisfied.

4.4.4 Covariance Simulation

Covariance simulations can provide estimates of state estimation error statistics without generating simulated noisy measurements. In this method, the covariance is propagated and updated in the standard Maximum *A-Posteriori* manner:

$$P_j = \left[\widetilde{H}_j^T \widetilde{R}^{-1} \widetilde{H}_j + P\right]^{-1} \tag{41}$$

but the state is *not* estimated. The statistics of the estimation method can be accurately determined if the true state is known, as is the case with truth-model simulations. Issues such as nonlinear convergence and estimator pull-in range are not considered in this method. Therefore, the covariance simulations constitute a lower-bound on the estimation error covariance. Fortunately, testing with the previously discussed estimator showed that the nonlinear nature of this system is mild, and the estimator converges on a very consistent basis. Therefore, the covariance simulation results presented in this paper are a good representation of the expected performance of the estimator when many different realizations of the system are averaged together.

5 Results

The previously described equations were implemented in a MATLAB simulation and the results of that simulation are provided here in the form of a parametric trade study.

5.1 Parametric Trade Study

This study explores the following quantities for the trade-space of an asteroid flyby: measurement type, asteroid classification, asteroid size, and spacecraft-asteroid relative flyby velocity. Three different measurement classes are considered: a camera, a camera and radar, and a lidar. Four different asteroid classes are examined: C (carbonaceous chondrite), S (chondrite), M (metallic), and P, with densities[2] of 1.0, 2.0, 4.0, and 0.8 g/cm^3, respectively. The asteroid sizes vary from a radius of 0.1–10 km, and the flyby speed spans 5–15 km/s.

5.1.1 Success Criteria

The trade-space is cast in terms of the number of probes required to satisfy a given error requirement. This study uses the 1 σ estimation error standard deviation associated with the asteroid's gravitational parameter as the metric, and sets the threshold to be 5% of the true value. For example, if four probes provide an estimate of the asteroid's gravitational parameter that is accurate to only 10% (1 σ) of its true value, then the number of probes are increased until the estimation error standard deviation is less than or equal to 5% . The maximum number of probes that could be used in any one flyby was limited to 100 probes.

5.1.2 Deployment Budget and Methodology

The probes are deployed from the host spacecraft prior to the asteroid flyby. Earlier deployments require less deployment Δv, while later deployments allow less time for errors to accumulate. The approach taken in this study was to identify many of the sources of error in the deployment process and combine them in a root-sum-of-squares approach. This approach assumes an unbiased Gaussian error model for each error source. Table 2 summarizes the deployment budget and the approximate expected magnitude of each error. The derivation and equations used to compute each quantity is omitted for the sake of brevity, but they are mostly derived from simple linearizations of nonlinear equations. The final deployment standard deviation using these approximations is 5.3 kilometers for a deployment 1.75 days prior to close-approach.

For the purposes of a trade-study, the probes were assumed to be deployed perfectly and in such a way that they created a ring about the asteroid at their closest approaches. This eliminates variation associated with stochastic deployment errors. The probes were simulated to pass the asteroid at 15 kilometers above the equivalent spherical radius of the asteroid. The 15 kilometers act as a buffer that is approximately 3 σ of the deployment budget, allowing for a significant deployment error. It is very unlikely that any of the probes will impact the asteroid. A perfect

Table 2: Deployment control budget components for a flyby speed of 15 km/s, a deployment speed of 3 m/s, and a lead time of closest approach of 1.75 days.

Error Source	**Error Magnitude**	**Propagated Error**
Spacecraft		
Relative Position Knowledge	3000 m	3000 m
Relative Velocity Knowledge	0.1 m/s	1512 m
Attitude Knowledge	5×10^{-5} rad	23 m
Deployment Mechanism		
Alignment Knowledge	8.7×10^{-3} rad	3959 m
Impulse Knowledge	0.001 m/s	151 m
Timing Knowledge	0.001 s	15 m
Environment		
Mismodeled Accelerations	1×10^{-7} m/s^2	1143 m

deployment will not occur in practice, but even the non-ideal deployments will provide similar results for a very high percentage of the samples of the stochastic (Gaussian) deployment budget.

5.1.3 Baseline Simulation Parameters

The simulation parameters used in the baseline scenario are listed in Table 3. The range of the camera, radar, and lidar were derived from several known instrument designs. The camera baseline is the Long Range Reconnaissance Imager[25] (LORRI) that is on the New Horizons spacecraft. Given a one second integration time, a 10 cm diffuse sphere is observable at 2000 km. For this duration, the imager is sensitive enough to identify stars of at least 15th magnitude, which improves the measurement accuracy by removing spacecraft pointing uncertainty. The radar is taken to be Ku band pulsed transmitter with 20W peak power for 400 μs. The antenna is a 1.5 m parabolic dish, which could be dual-purposed as the spacecraft's communications high-gain antenna. For a 10 cm retroreflector assembly, this radar could achieve detection at roughly 200 km. The lidar is modeled as a 1064 nm source with 0.5 mJ, 5 ns pulses and a beam divergence of 0.1 mrad. These values are not unlike the laser altimeter flown on the Near Earth Asteroid Rendezvous Mission.[26] The silicon avalanche photodiode detector can operate in one of two modes: linear amplification and Geiger mode. The linear mode, which is traditionally used, offers ranges of roughly 200 km to a 10 cm retroreflector. The Geiger mode is extremely sensitive, achieving detection ranges of over 2000 km, but generates false-positives that must be reduced statistically by integrating multiple returns and cooling to reduce thermal noise.

The trajectory of the host spacecraft and the probes is depicted in Figures 4 and 5. The host spacecraft is at bottom of the figure, the asteroid is in the top right, and the probes are arranged in a ring and are about to pass-by the asteroid. The figure is meant as a visualization aid only;

Table 3: Simulation parameters used for the trade-study.

Simulation Parameter	**Value**
A priori asteroid mass estimate (1 σ)	100%
Simulation duration	10 days
Time between measurements	10 minutes
Spacecraft/asteroid closest approach	500 km
Probe position deployment accuracy (1 σ)	1 m
Probe velocity deployment accuracy (1 σ)	0.1 m/s
Camera angular measurement accuracy (1 σ)	0.75/3600 deg
Camera maximum measurement range	2000 km
Radar range measurement accuracy (1 σ)	0.5 m
Radar velocity measurement accuracy (1 σ)	1 m/s
Radar maximum measurement range	200 km
Lidar angle measurement accuracy (1 σ)	0.1 mrad
Lidar range measurement accuracy (1 σ)	10 cm
Lidar maximum measurement range	2000 km
Asteroid density, C Class	1.0 g/cm^3
Asteroid density, S Class	2.0 g/cm^3
Asteroid density, M Class	4.0 g/cm^3
Asteroid density, P Class	0.8 g/cm^3

none of its components are to scale.

5.1.4 Baseline Results

The number of probes that are needed to estimate the asteroid's gravitational parameter to a 5% threshold with the given set of parameters is shown in Figure 6. The number of probes required for each parameter combination is depicted by the color. The white area indicates that the maximum considered quantity of 100 probes were insufficient to recover the gravity information to to the required threshold. The number of probes needed to accurately estimate the gravitational parameter decrease as the asteroid increases in size, as the flyby speed decreases, and as the density increases. The rows of contour plots each indicate the type of tracking used (camera, camera and radar, or lidar). The columns of contour plots indicate the class of the asteroid that is being considered (C, S, M, or P).

Figure 7 shows the results of the same computation, but using the estimation error threshold on the g_2 term, which corresponds to the first zonal harmonic, J_2. The point-mass term can be more readily estimated than the g_2 term because its effect drops-off at a rate proportional to r^{-2} instead of r^{-3}. Several probes are always required to estimate the g_2 term.

5.1.5 Time-Dependence Estimation Results

The accuracy of the estimation results improves as the probes are tracked for a longer period of time after the flyby. Figure 8 has been included to illustrate this point, which gives estimation accuracy as a function of time. The results are shown for the camera and the lidar using the simulation parameters mentioned previously. The combined radar and camera case is identical to the camera-only case in performance, owing to the radar's short effective range. In this simulation the spacecraft is moving *parallel* to the probes past a 1.0 km radius asteroid with a closest-approach of 500 kilometers and a flyby velocity of 10 km/s. With the camera and lidar, the host spacecraft can always detect the probes.

The estimation error begins at 100% because it is assumed that the asteroid's gravitational parameter can be estimated to at least that well using *a priori* information, i.e., before any measurements are taken of the probes. The simulation was ended after 8 days because it is very likely that mismodeled accelerations, such as solar radiation pressure, will accumulate sufficiently to degrade the estimation results. The accuracy in the figure improves dramatically once the flyby occurs, near 1 day. The improvement is very significant over a time-span of approximately 1/2–1 day for the lidar case but requires more time for the camera. This observation motivates a second trade-study, one with a series of maneuvers that bring the spacecraft closer to the probes and keeps them in close proximity for a significant amount of time.

5.1.6 Trade-Study Results from a Scenario with a Maneuver

This trade study uses the maneuver portrayed in Figure 9. The spacecraft starts approaching the target asteroid directly. A small thrust is performed to move the spacecraft downward in the figure, then an equal thrust is provided in the opposite direction to move halt the spacecraft's lateral motion with respect to the asteroid. This second maneuver occurs once the spacecraft has moved sufficiently distant that it is in no danger of collision with the asteroid. Once the flyby occurs another thrust is performed to move the spacecraft upward in the figure. Once the spacecraft has come close to the probes the thruster is again used to halt the spacecraft's lateral motion. The distance between the host spacecraft and the asteroid at flyby was approximately 500 kilometers, and the distance between the centroid of the probes and the host spacecraft post flyby was approximately 75 kilometers. Each thrust can be very small if the first one is initiated far in advance. This simulation used a Δv of 10 m/s for each thrust, but half of that amount, or even less, would be possible. The sensor resolutions are the same as in the previous no-maneuver case, but their effective range requirements are significantly reduced: a range of 100 kilometers for the camera and radar, and 200 kilometers for the lidar. These reduced range requirements are easily met with heritage sensors.

Figures 10 and 11 show the results of the trade study, but for the case when the spacecraft maneuvers. As expected, the estimation algorithm is typically able to more accurately determine the gravitational parameters.

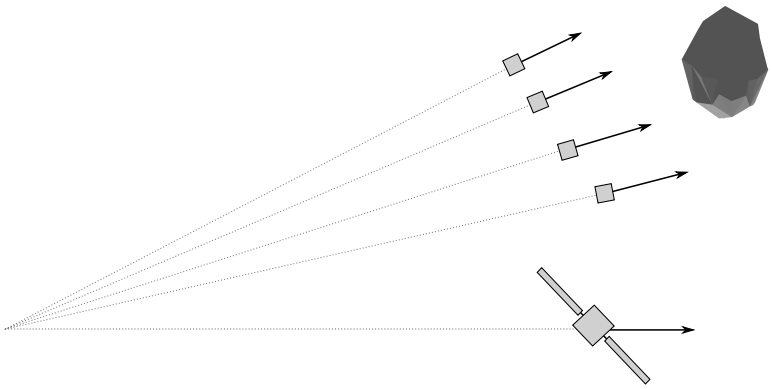

Figure 4: Top view of baseline deployment of ring of probes.

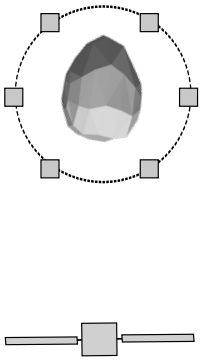

Figure 5: View along host spacecraft velocity at time of close-approach.

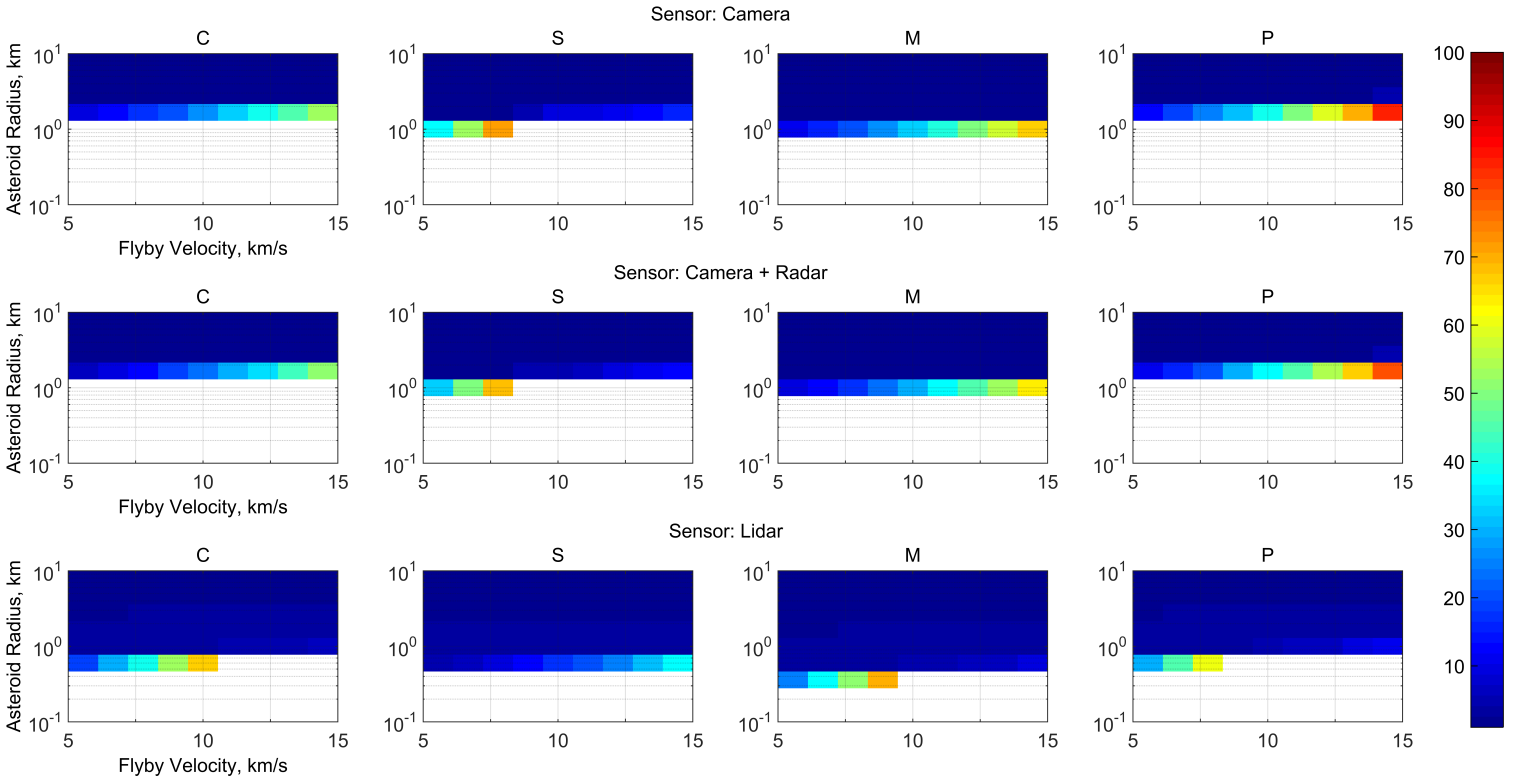

Figure 6: The number of probes needed to estimate the point-mass gravity term to better than 5%.

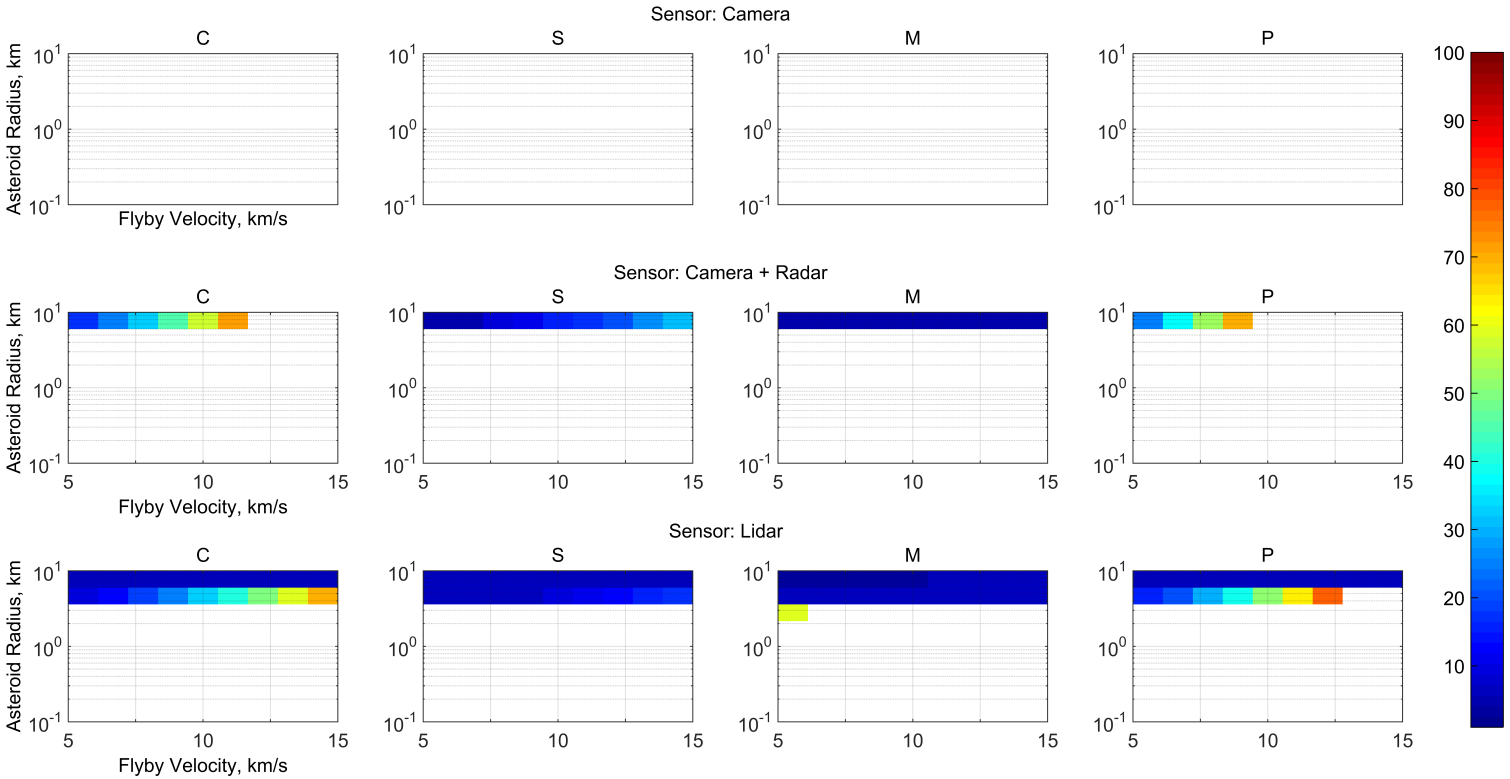

Figure 7: The number of probes needed to estimate the J_2 gravity term to better than 5%.

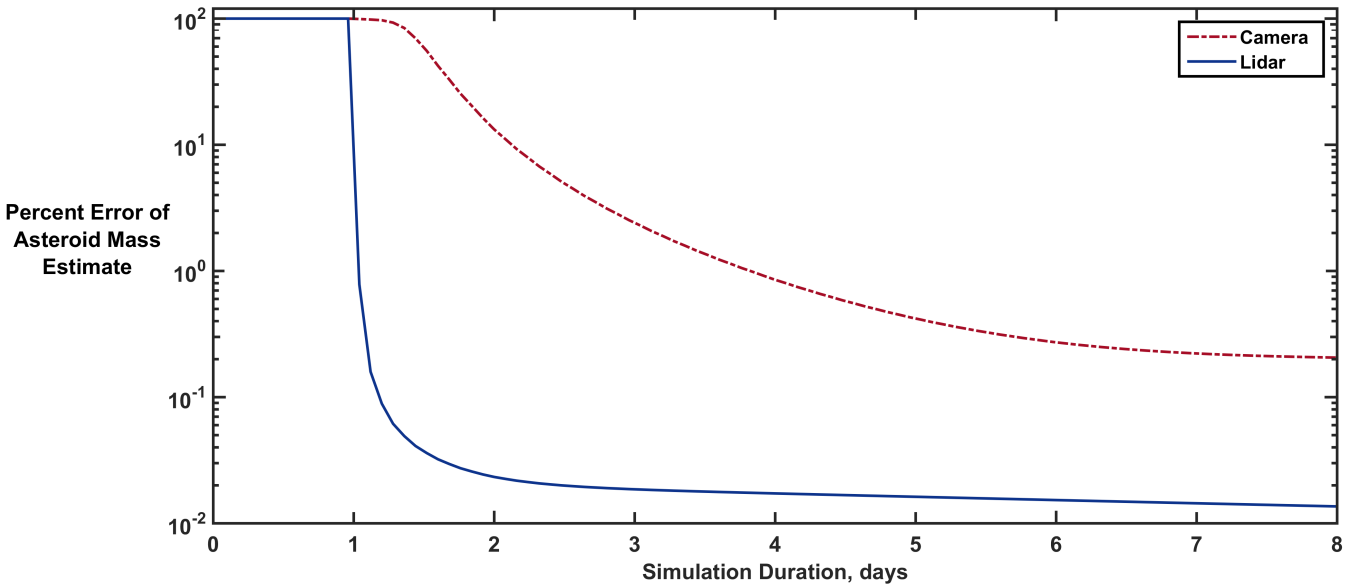

Figure 8: Accuracy of the point-mass gravitational parameter estimate versus simulation/tracking time.

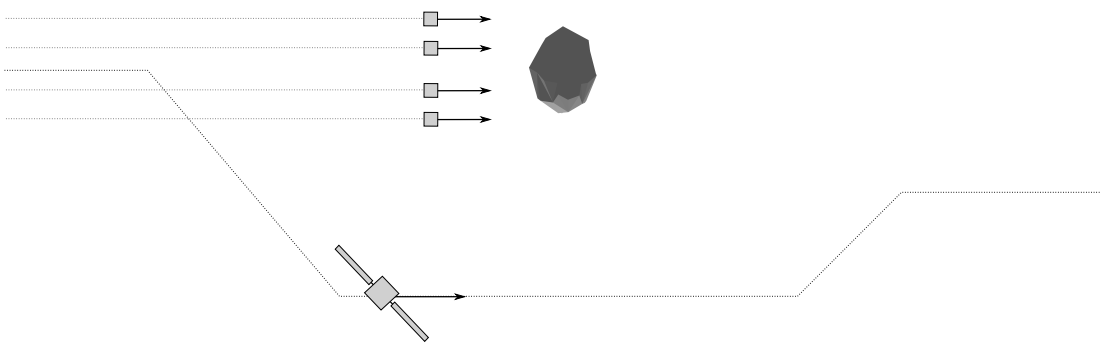

Figure 9: Top view of maneuvered deployment of ring of probes.

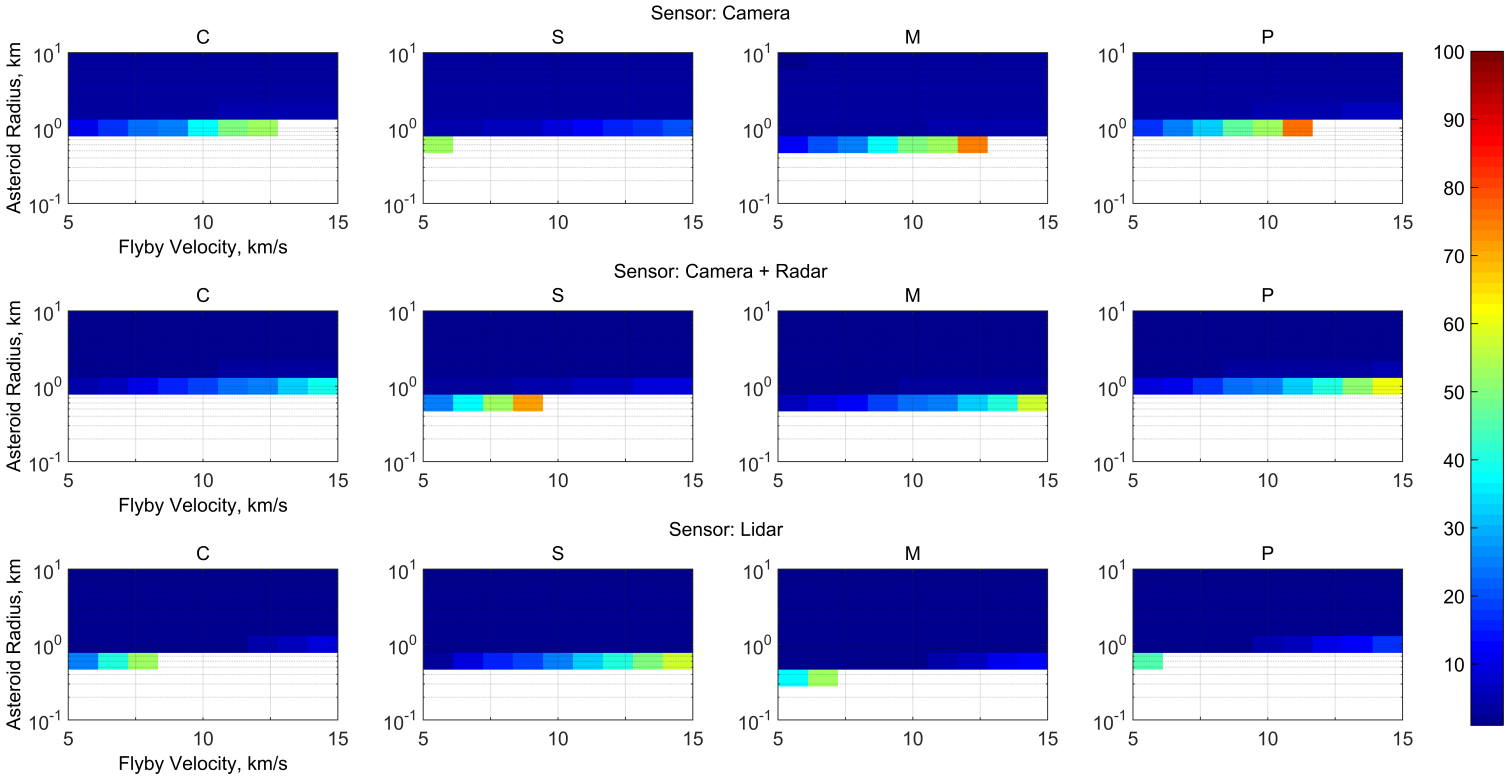

Figure 10: The number of probes needed to estimate the point-mass gravity term to better than 5% when a maneuver is used.

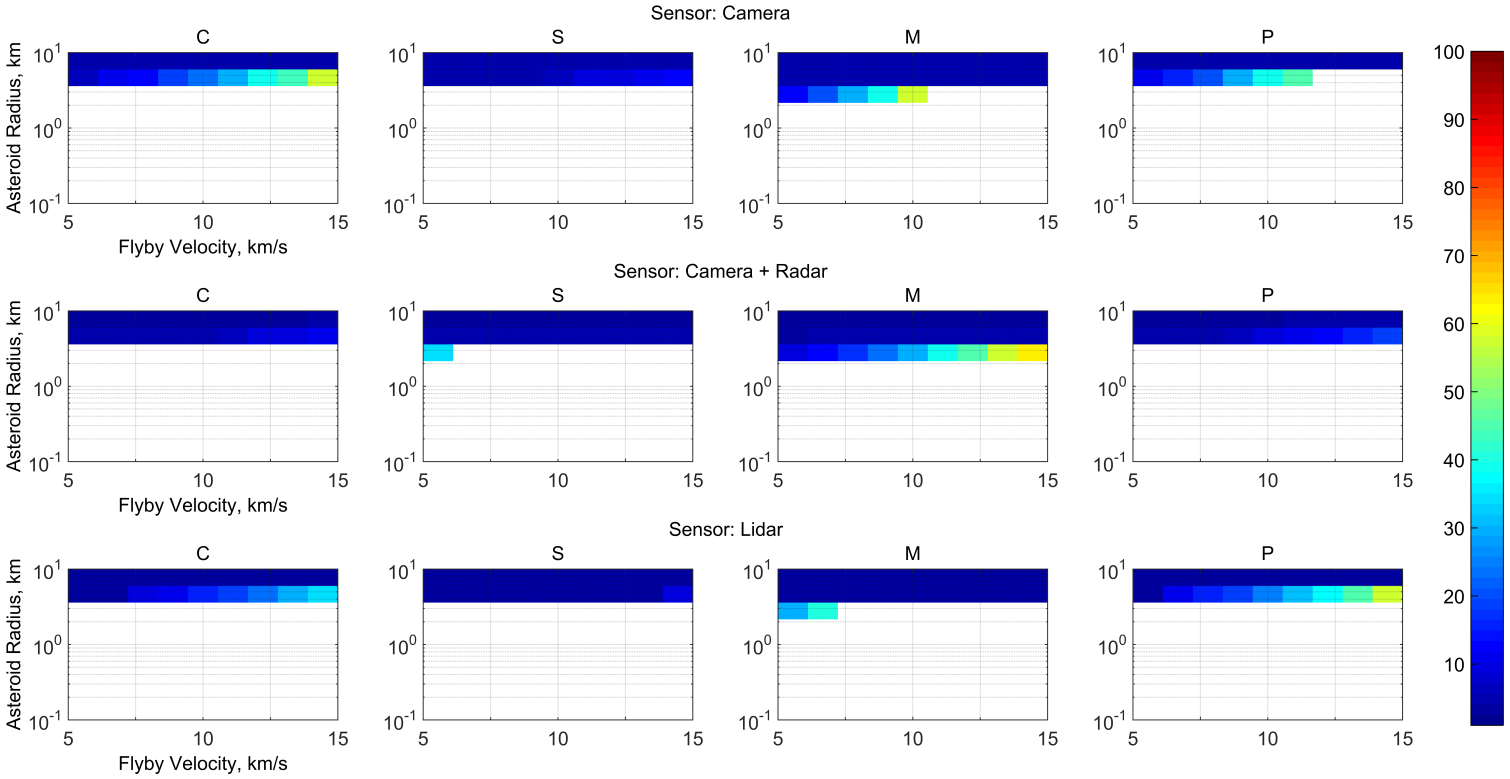

Figure 11: The number of probes needed to estimate the g_2 gravity term to better than 5% when a maneuver is used.

5.2 Flyby Tour Example

An example flyby tour was generated to illustrate the effectiveness of the technology in a realistic mission context. In this case, the spacecraft is launched into a trajectory that is roughly tangent with the inner main belt asteroids. This approach has the advantage of yielding many slow (4-8 km/s) flybys. The launch is low energy (C_3 of 21.0 km^2/s^2) consistent with small class Atlas or Delta launch vehicles. The trajectory includes 8 asteroid flybys in 4.7 years (3 apoapse passes). Shortly after each flyby, the spacecraft executes a trajectory correction maneuver to target the next flyby. The total Δv is 1950 m/s, which is within the range of many current small spacecraft missions. As a reference, if the spacecraft were launched on an Atlas V 401 vehicle and were equipped with a bipropellant hydrazine propulsion system, it would have an available wet-mass of 1830 kg and dry-mass of 974 kg. In short, this design would be readily feasible for a NASA Discovery class mission. The trajectory is shown in Figure 12.

The flybys are listed in Table 4. Little is known about these targets, other than their absolute magnitude. In the absence of other information, it can reasonably be assumed that they are S-type asteroids, since those are the most common type in the solar system. Given this, we can estimate the mean size of the object using published absolute magnitude values and a representative S-type V-band albedo of 0.19.[27] The resulting sizes are relatively small compared to the sizes shown to be effective in the trade-studies illustrated in Figures 6-7.

The most feasible of the tracking methods is the approach that uses an on-board camera to image diffuse spheres against the star background. This could be easily implemented on a typical spacecraft. There are a variety of TRL 9 options that would be compatible with this approach, including LORRI as was used in the trade-study above.

Table 4: Flyby bodies in asteroid tour mission.

	Name	**Abs. Magnitude**	**Radius, km**	**Flyby Speed, km/s**
1	1998 TN30	15.1	1.47	6.32
2	2000 QY95	16.2	0.89	8.08
3	1996 BZ3	18.1	0.37	5.13
4	2007 TT32	17.8	0.43	5.88
5	2006 UA71	17.0	0.61	5.40
6	2002 TH273	17.4	0.51	6.36
7	2004 FR38	17.1	0.59	4.45
8	1998 ST96	17.6	0.47	4.86

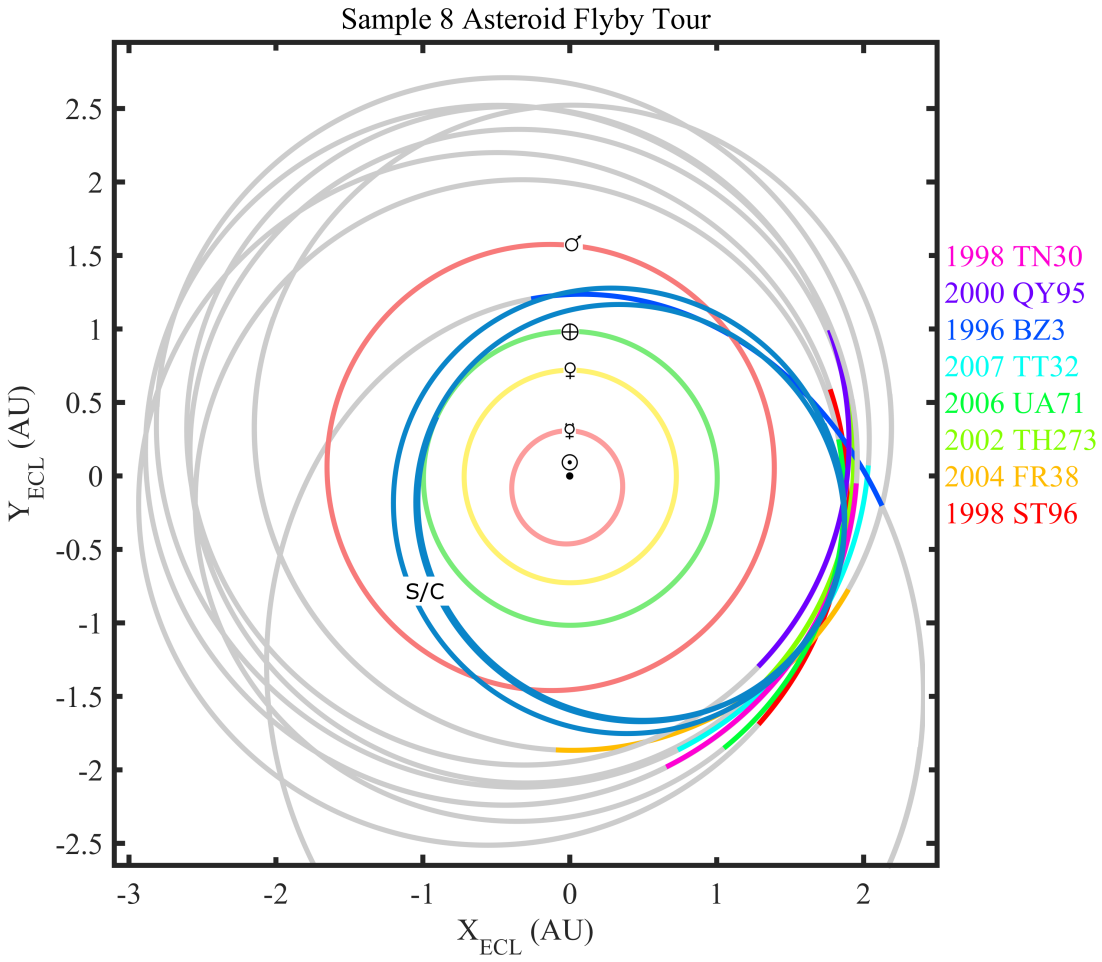

Figure 12: Sample 8 flyby trajectory. The asteroid flybys occur in the inner main-belt. The spacecraft completes 3 orbits. Each of the flyby asteroid orbits is colored for +/- 90 days around the flyby event.

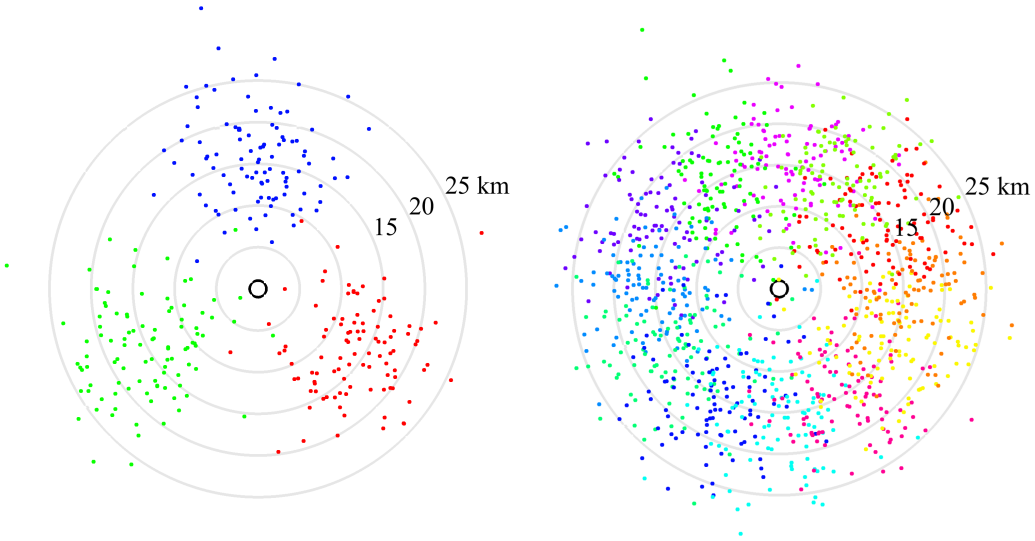

Figure 13: Representative random samples from the deployment budget for (a) 3 probe positions and (b) 12 probe positions. Concentric rings of 5 km increments are shown.

In the case of the trade-study, the probes were deployed with perfect accuracy in a ring with an altitude of 15 km above the surface of the asteroid. For this example mission, each probe is deployed with the same nominal ring configuration, albeit with a random error consistent with the deployment budget given in Table 2. In order to characterize the effects of the deployment uncertainty on the results, 20 simulations were conducted, each with a random draw from the deployment statistics. This is illustrated in Figure 13, which shows 100 representative draws from the deployment budget for 3 and 12 probe deployment target positions. The concentric circles show range from asteroid center in 5 km increments.

Two sets of results are presented in Table 5. The first set includes the case of a host spacecraft deploying 3 probes per asteroid flyby. In this case, the results are highly dependent on the delivered flyby location of the probes. In deployment cases where the close-approach range for at least one of the probes is very low, the results show point-mass estimates with less than 5% uncertainty. In deployment cases where the close-approach range for all the probes is comparatively high, the measurements do not offer useful observability for the asteroid's mass.

Given the importance of delivering a probe to a low altitude, the second set of results addresses the case of a host spacecraft deploying 12 probes per asteroid flyby. Here, the higher number of probes is intended to increase the likelihood of any one probe achieving a low altitude. The results are significantly improved, with the mean uncertainty less than 15% for most cases. A 15% error would represent a valuable measurement for many asteroid applications.

Though not simulated here, one could consider a potentially riskier approach, where the host would attempt to deploy the probes directly at the asteroid, recognizing that errors will tend to make the probes miss the asteroid and pass at close ranges. For a 1 km asteroid and the deployment budget used here, one would expect only 1 in roughly 175 probes to impact the asteroid. The operational risk is that the error budget could be conservative, in which case the odds of impact would be higher. Even so, if the errors were halved, only 1 in 45 probes would be predicted to impact.

Table 5: Sample point-mass results for 20 simulations of the example asteroid flyby mission deploying 3 or 12 probes.

		Point Mass Percent Uncertainty					
		3 Probes			**12 Probes**		
	Name	**Min**	**Mean**	**Max**	**Min**	**Mean**	**Max**
1	1998 TN30	0.2	9.4	53.9	< 0.1	2.9	10.6
2	2000 QY95	0.9	12.7	64.8	0.3	4.9	19.8
3	1996 BZ3	7.6	27.9	58.2	4.0	23.2	49.3
4	2007 TT32	3.6	33.7	96.0	1.5	19.5	66.5
5	2006 UA71	0.3	22.0	86.6	< 0.1	7.5	30.4
6	2002 TH273	0.8	23.2	70.6	< 0.1	13.9	46.2
7	2004 FR38	0.9	22.7	80.8	0.3	8.6	22.7
8	1998 ST96	2.5	31.2	72.4	1.1	12.4	27.6

6 Conclusions

The mass of small bodies in the solar system is a relevant but challenging measurement to obtain. This analysis indicates that the point-mass term of small bodies larger than roughly 500 m in diameter can be observed from a host spacecraft that tracks locally deployed probes throughout a flyby to an uncertainty of better than 5%. Of the estimated asteroid populations, this suggests that gravimetry would be useful for roughly 3000 near-Earth asteroids,[28] 10^7 main-belt asteroids[29] and the vast majority of known comets.[30] The conditions by which this measurement is possible depends on the characteristics of the asteroid (size, type), the flyby velocity, and the type of tracking available (angles-only or angles+ranging). This analysis indicates that a few (1-3) probes can be very effective for most encounters, with marginal improvement for additional probes. However, given practical deployment errors, the system may need to deploy many probes to ensure that at least a few arrive close to the target body. The solution accuracy is sensitive to the amount of post-encounter time that the probes are tracked. For some instruments, particularly angles-only methods, this may require that the host spacecraft maneuver in order to continue tracking the probes for meaningful durations (roughly 2-5 days). Long duration tracking of probes flying by large asteroids (>5 km diameter) can sometimes provide observability of the gravity field's first spherical harmonic, J_2. In summary, this method offers a feasible approach to augmenting flyby science.

7 Next Steps

The analysis to-date has focused on establishing feasibility in practical mission contexts. Having determined that the approach is feasible under reasonable assumptions, there are a variety of compelling follow-on activities for this research. These activities can be divided into three broad categories: Additional Applications, Simulation Fidelity, and Implementation Readiness.

7.1 Additional Applications

The research to date has focused on exploring asteroid flybys by spacecraft on interplanetary trajectories. There are a variety of other relevant applications or scenarios that the technique could impact.

7.1.1 Binary Flybys

Approximately 16% of Near-Earth asteroids over 200 m in diameter are thought to be binary systems (two asteroids co-orbiting a barycenter).[31] In this case, the mass of the system can be estimated by observing the orbital period of the two objects. This type of target would make an excellent experimental "control" for swarm flyby gravimetry, in that there would two independent methods of determining the gravity. That said, one would need to analyze the gravimetry concept in such a system, and characterize the system performance when there are two massive bodies in the system.

7.1.2 Planetary Systems

Many flyby missions operate within planetary systems, such as Galileo at Jupiter, Cassini at Saturn, or the proposed Clipper mission at Jupiter. Here, the spacecraft orbits the central planet in resonance orbits with moons of interest. The spacecraft collects science on the moon during the short flyby period. These flybys have produced gravity models for many moons, giving insight into interior composition. In the case of the proposed Clipper mission, gravity science is attempting to help understand subsurface ocean depths and properties of Europa. This science is being achieved using the recently developed Deep Space Atomic Clock. Even so, the measurements and observability are limited. Swarm flyby gravimetry could potentially be a feasible, low-cost means of improving this type of science.

7.1.3 Collaborative Tracking

If the flyby encounter were near enough to Earth, it's conceivable that the ground-based assets could participate in the gravimetry measurement. For example, one could include radar observations from Arecibo or VLBI acting independently or as a component of a bistatic system.

7.1.4 Flybys of Bodies that Outgas or have Atmospheres

When flying by a moon with an atmosphere (e.g. Titan) or comet that is outgassing, the probe's orbit will be perturbed by atmospheric drag or outgassing. It may be possible to estimate these accelerations in addition to the body's gravity. This estimate would represent an observation of atmosphere density, possibly measured at a variety of altitudes simultaneously.

7.1.5 Second Order Measurements

Dr. Brin of the NIAC External Council suggested that the probes could be designed to offer measurements via gravity-gradient torques. Here, two probes would be connected by a thin tether and the orientation time-history would be used as a second measurement type. This, and other second order measurements, may represent additional observations into the small body's unknown gravity field.

7.2 Simulation Fidelity

7.2.1 Accelerations

The current simulation has a number of assumptions and limitations that should be addressed. In terms of modeling accuracy, it lacks the following accelerations:

1. "Third-body" acceleration from additional bodies, e.g. Sun and Jupiter
2. Solar radiation pressure
3. Higher order gravitational terms associated with the asteroid, i.e. beyond J_2
4. Relativity, especially for higher flyby velocities

In some instances, it may also be useful to quantify or simulate acceleration contributions associated with comet outgassing, radiant acceleration due to reflected sunlight or thermal emission, dust impacts, ant atmospheric drag.

Finally, in operation, one would use a known or generated shape model for the small-body that the asteroid passed. These are typically generated using the host spacecraft's on-board imager. Given this, the estimation algorithms would directly estimate the density of the object, rather than the mass. That is, the partial derivatives would be associated with the acceleration with respect to a constant density. One could even consider other parameterizations of density, which would be applicable for moons within planetary systems. For example, one could attempt to estimate the density of an inner core and an outer shell of ice. This possibility is discussed more in Section 7.1.2.

7.2.2 Numerical Stability

For poorly performing flyby scenarios, the numerical conditioning of the problem can yield erroneous results. Currently, we accommodate these cases by checking the condition number of certain key matrices and excluding any results that violate a predefined value. However, a more appropriate approach is to use a square-root information implementation of a nonlinear Bayesian estimator, such as an extended Kalman Filter. These types of algorithms are known to give a square-root improvement in condition number and enable better numerical conditioning. In addition to improving the quality of the result, this will enable the deployment optimization study described in Section 7.2.4, the results of which are currently limited by numerical issues.

7.2.3 Coordinate Selection

The baseline simulation was constructed in Cartesian coordinates. For angles-only tracking there is evidence[32] showing that curvilinear coordinates improve observability. It would be prudent to assess the benefits of this approach for the highly hyperbolic flyby case.

Additionally, the simulation is currently constructed using a frame that is located at the center of a fixed-velocity asteroid. In truth, the asteroid's path is nonlinear, owing to the sun's gravity. As we increase the fidelity of the models, the system should be modeled in a truly inertial frame.

7.2.4 Deployment Optimization

The current trade-study and example mission used a "ring" deployment approach, in which the probes were deployed in a circle centered at the asteroid. Although this approach is intuitive, it doesn't incorporate known sensitivities associated with measurement range, duration, or type. For example, deploying a probe on the far side of the asteroid, while giving unique observability into the far side's gravity, suffers from poorer measurement accuracy and shorter measurement duration (since it is drifting away from the host faster). Additionally, if its motion is coplanar with the host, there is high observability into the gravitational perturbation using range measurements and poor observability using angles-only measurements. An optimized deployment approach would incorporate these detrimental factors and select a location that maximized the information provided by the measurement set while accounting for expected deployment errors.

7.3 Implementation Readiness

Although the deployment and tracking methods are likely feasible, there remain a number of key concerns that should be readily addressed.

7.3.1 Target and Star Rendering for Camera

The angles-only tracking associated with the camera is enabled by its high accuracy. This accuracy results from the ability to co-image the target and a background star-field. There is a possibility

that there will be insufficient stars to accurately locate the probe, particularly at short integration times before the probe has passed the asteroid. This could be resolved using a medium-to-high fidelity scene renderer, which would model the telescope, focal plane, target, star-field, and glare. This software has been developed for other programs at JHU/APL, but has not been applied to this particular case.

7.3.2 Lidar Geiger Mode

The long range tracking of the Lidar was enabled by a so-called Geiger mode, in which the Lidar's avalanche photodiode responds to as few as a single photon. This gives detection sensitivities out to beyond 2000 km. To our knowledge, this mode has not been operated on a spacecraft. The challenge is that some portion of background light or thermal noise will generate false-positives. That is, it is so sensitive that it will sometimes report a detection and range when none has occurred. To reduce thermal noise, one can cool the photodiode, though this comes at a non-trivial cost to implement on-board a spacecraft. This would need to be assessed to identify what options, including passive cooling, are available. To reduce background light, a narrow filter can be used on the receiving optics. Additionally, one can use something called "range-gating", in which the photodiode is left inactive except for a short period when one expects to receive a true return. This is equivalent to filtering the incoming photons based on range. Even with this technique, there are false positives. However, this rate can be assessed by looking at a blank portion of sky and determining the background level of signal. Another approach, which has not been implemented to our knowledge, is to use techniques from signals-processing where a known time-series of pulses are transmitted and then searched for. This is analagous to pseudorandom codes used in GPS detection and tracking. Here, a time-independent (e.g. white noise) background can be separated from the time-dependent signal. The eventual goal is to develop a statistical hypothesis test for this measurement approach.

7.3.3 Unfolding Retroreflector

The unfolding retroreflector design illustrated in Figure 2 represents a compact way to store an axisymmetric (attitude independent), high reflectivity target probe shape. In it, a set of 8 mirrors would unfold to produce a set of 8 corner-cube retroreflectors oriented to form a sphere. There is some concern that the tolerances required for Lidar returns are too stringent for a folding design. It would be straightforward to characterize or even test these tolerances to identify the sensitivity of surface smoothness and orientation to detectability. Pending this investigation, we would continue to consider additional designs.

7.3.4 Deployment Accuracy

The control and knowledge of the deployment state of the probe is very relevant to the system's performance. From the stand-point of control, the example mission demonstrated that expected

uncertainties can significantly affect the results, insomuch as distant probe flybys give little to no useful information. In terms of knowledge, the angles-only tracking method used by the camera is sensitive to the initial uncertainty. For example, if no information were available, the method would likely be unobservable for any probe flyby configuration. To this end, it would be useful to better assess and test the dispenser design. It would be straightforward to purchase and test the linear motor, which is relatively inexpensive, to identify the expected repeatability of the deployment. This test would inform the deployment error budget, which is a key parameter in the simulations.

8 Acknowledgments

The authors wish to thank Clint Apland, Jonathan Bruzzi, Zachary Fletcher, Bob Jensen, and Kim Strohbehn of the Johns Hopkins University Applied Physics Laboratory for subject matter expertise with regards to tracking methods and hardware implementations.

9 References

[1] G. Consolmagno, D. Britt, and R. Macke, "The Significance of Meteorite Density and Porosity," *Chemie der Erde-Geochemistry*, Vol. 68, No. 1, 2008, pp. 1–29.

[2] B. Carry, "Density of asteroids," *Planetary and Space Science*, Vol. 73, No. 1, 2012, pp. 98–118.

[3] D. Yeomans, P. Chodas, M. Keesey, W. Owen, and R. Wimberly, "Targeting an asteroid–The Galileo spacecraft's encounter with 951 Gaspra," *The Astronomical Journal*, Vol. 105, 1993, pp. 1547–1552.

[4] D. W. Dunham, J. V. McAdams, and R. W. Farquhar, "NEAR Mission Design," *Johns Hopkins APL Technical Digest*, Vol. 23, No. 1, 2002, pp. 18–33.

[5] D. Ragozzine, "Collectible Projectosats," *NIAC Annual Meeting, Student Visions of the Future Program*, October 2004.

[6] J. A. Atchison, Z. R. Manchester, and M. A. Peck, "Swarm Augmented Flyby Gravimetry (Poster)," *9th IAA Low Cost Planetary Missions Conference, Laurel MD*, June 2011.

[7] C. B. Grosch and H. R. Paetznick, "Method of Deriving Orbital Perturbing Parameters from Onboard Optical Measurements of an Ejected Probe or a Natural Satellite," Tech. Rep. CR-1412, NASA Langley Research Center, August 1969.

[8] M. L. Psiaki, "Absolute Orbit and Gravity Determination using Relative Position Measurements Between Two Satellites," *Journal of Guidance, Control, and Dynamics*, Vol. 34, No. 5, 2011, pp. 1285–1297.

[9] E. S. Muller and P. M. Kachmar, "A New Approach to On-Board Orbit Navigation," *Journal of the Institute of Navigation*, Vol. 18, No. 4, 1971-72, pp. 369–385.

[10] T. Tanaka and Y. Kawamura, "Overview and Operations of Cubesat FITSAT-1 (NIWAKA)," *IEEE - Recent Advances in Space Technologies, Istanbul*, June 2013, pp. 887–892.

[11] B. D. Tapley, S. Bettadpur, M. Watkins, and C. Reigber, "The Gravity Recovery and Climate Experiment: Mission overview and early results," *Geophysical Research Letters*, Vol. 31, No. 9, 2004.

[12] T. L. Hoffman, "GRAIL: Gravity Mapping the Moon," *Aerospace conference, 2009 IEEE*, IEEE, 2009, pp. 1–8.

[13] E. I. Keroglou, "Analysis and design of retroreflectors," tech. rep., Master's Thesis, US Naval Post Graduate School, 1997.

[14] P. A. Bernhardt, A. Nicholas, L. Thomas, M. Davis, C. Hoberman, and M. Davis, "The Precision Expandable Radar Calibration Sphere (PERCS) With Applications for Laser Imaging and Ranging," tech. rep., Naval Research Laboratory, DTIC Report, 2008.

[15] D. Mott, "On the radar cross section of a dipole," *Proceedings of the IEEE*, Vol. 58, No. 5, 1970, pp. 793–794.

[16] C. Overhage and W. Radford, "The Lincoln Laboratory West Ford Program - An Historical Perspective," *Proceedings of the IEEE*, Vol. 52, No. 5, 1964, pp. 452–454.

[17] T. Kailath, *Linear Systems*. Prentice-Hall, 1980.

[18] O. Montenbruck and E. Gill, *Satellite Orbits*. Springer, 2000.

[19] J. R. Dormand and P. J. Prince, "A family of embedded Runge-Kutta formulae," *Journal of computational and applied mathematics*, Vol. 6, No. 1, 1980, pp. 19–26.

[20] R. J. Lopez, *Advanced engineering mathematics*, Vol. 1158. Addison-Wesley, 2001.

[21] D. A. Vallado, *Fundamentals of Astrodynamics and Applications*. Microcosm Press, 3 ed., 2007.

[22] B. Tapley, B. Schutz, and G. Born, *Statistical Orbit Determination*. Burlington, MA: Elsevier Academic Press, 2004.

[23] B.-S. Yaakov, L. Rong, and K. Thiagalingam, *Estimation with applications to tracking and navigation*. John Wiley & Sons, Inc.: New York, NY, USA, 2001.

[24] P. Gill, W. Murray, and M. Wright, *Practical Optimization*. Academic Press, 1981.

[25] A. F. Cheng, H. Weaver, S. Conrad, and e. al., "Long-Range Reconnaissance Imager on New Horizons," *Space Science Reviews*, Vol. 140, October 2008, pp. 189–215.

[26] T. Cole, M. Boies, A. El-Dinary, A. Cheng, M. Zuber, and D. Smith, "The Near-Earth Asteroid Rendezvous laser altimeter," *The Near Earth Asteroid Rendezvous Mission*, pp. 217–253, Springer, 1997.

[27] A. N. Cox, ed., *Allen's Astrophysical Quantities*. Springer, 2000.

[28] J. S. Stuart and R. P. Binzel, "Bias-corrected population, size distribution, and impact hazard for the near-Earth objects," *Icarus*, Vol. 170, No. 2, 2004, pp. 295–311.

[29] E. F. Tedesco, A. Cellino, and V. Zappalá, "The statistical asteroid model. I. The main-belt population for diameters greater than 1 kilometer," *The Astronomical Journal*, Vol. 129, No. 6, 2005, p. 2869.

[30] K. Meech, O. Hainaut, and B. Marsden, "Comet nucleus size distributions from HST and Keck telescopes," *Icarus*, Vol. 170, No. 2, 2004, pp. 463–491.

[31] J.-L. Margot, M. Nolan, L. Benner, S. Ostro, R. Jurgens, J. Giorgini, M. Slade, and D. Campbell, "Binary asteroids in the near-Earth object population," *Science*, Vol. 296, No. 5572, 2002, pp. 1445–1448.

[32] J. Tombasco and P. Axelrad, "Observability of Relative Hybrid Elements, Given Space-Based Angles-Only Observations," *Journal of Guidance, Control, and Dynamics*, Vol. 35, No. 5, 2012, pp. 1681–1686.